

10-mega pixel snapshot compressive imaging with a hybrid coded aperture

ZHIHONG ZHANG^{1,2,†}, CHAO DENG^{1,2,†}, YANG LIU³, XIN YUAN^{4,*}, JINLI SUO^{1,2,*}, AND QIONGHAI DAI^{1,2,5}

¹Department of Automation, Tsinghua University, Beijing 100084, China

²Institute for Brain and Cognitive Science, Tsinghua University, Beijing 100084, China

³Computer Science and Artificial Intelligence Laboratory, Massachusetts Institute of Technology, Cambridge, Massachusetts 02139, USA

⁴Bell Labs, 600 Mountain Avenue, Murray Hill, New Jersey 07974, USA

⁵Beijing National Research Center for Information Science and Technology, Tsinghua University, Beijing 100084, China

*Corresponding author: xyuan@bell-labs.com, jlsuo@tsinghua.edu.cn

Compiled August 17, 2021

High resolution images are widely used in our daily life, whereas high-speed video capture is challenging due to the low frame rate of cameras working at the high resolution mode. Digging deeper, the main bottleneck lies in the *low throughput* of existing imaging systems. Towards this end, snapshot compressive imaging (SCI) was proposed as a promising solution to improve the throughput of imaging systems by compressive sampling and computational reconstruction. During acquisition, multiple high-speed images are encoded and collapsed to a single measurement. After this, algorithms are employed to retrieve the video frames from the coded snapshot. Recently developed Plug-and-Play (PnP) algorithms make it possible for SCI reconstruction in large-scale problems. However, the lack of high-resolution encoding systems still precludes SCI's wide application. In this paper, we build a novel hybrid coded aperture snapshot compressive imaging (HCA-SCI) system by incorporating a dynamic liquid crystal on silicon and a high-resolution lithography mask. We further implement a PnP reconstruction algorithm with cascaded denoisers for high quality reconstruction. Based on the proposed HCA-SCI system and algorithm, we achieve a 10-mega pixel SCI system to capture high-speed scenes, leading to a high throughput of 4.6G voxels per second. Both simulation and real data experiments verify the feasibility and performance of our proposed HCA-SCI scheme. © 2021 Optical Society of America

<http://dx.doi.org/10.1364/ao.XX.XXXXXX>

1. INTRODUCTION

Recent advances of machine vision with applications in robotics, drones, autonomous vehicles and cellphones have driven high resolution images into our daily life. However, high-speed high-resolution videos though having wide applications in various fields such as physical phenomenon observation, biological fluorescence imaging, live broadcast of sports, on the other hand, are facing the challenge of *low throughput* due to the limited frame rate of existing cameras working at the high resolution mode. This is further limited by the memory, bandwidth and power. This paper aims to address this challenge by building a high-speed high-resolution imaging system using compressive sensing. Specifically, our system captures the high-speed scene in an encoded way and thus maintain the low bandwidth during capture. After this, reconstruction algorithms are employed to reconstruct the high speed high resolution scenes to achieve high throughput. Note that though the idea of video compressive sensing has been proposed before, scaling it up to 10-mega pixel in spatial resolution presents the challenges of both hardware implementation and algorithm development. Please refer to Fig. 1 for a real high-speed scene captured by our

newly built camera.

While 10-mega pixel lenses and sensors are both accessible, the main challenge for high-speed and high-resolution imaging lies in the deficient processing capability of current imaging systems. Massive data collected from high-speed high-resolution recording imposes dramatic pressure on the system's storage and transmission modules, and thus makes it impossible for long-time capturing. In recent decades, the boosting of computational photography provides researchers with creative ideas and makes breakthroughs in many imaging-related fields like super-resolution [1–3], deblurring [4–6], depth estimation [7–9] and so on. Regarding the *high throughput imaging*, snapshot compressive imaging (SCI) has been proposed and become a widely used framework [10–12]. It aims to realize the reconstruction of high-dimensional data such as videos and hyper-spectral images from a single coded snapshot captured by a two-dimensional (2D) detector. A video SCI system is typically composed of an objective lens, a *temporally varying* mask, a monochrome or color sensor, and some extra relay lenses. During every single exposure, tens of temporal frames are modulated by corresponding temporal-variant masks and then integrated into a single

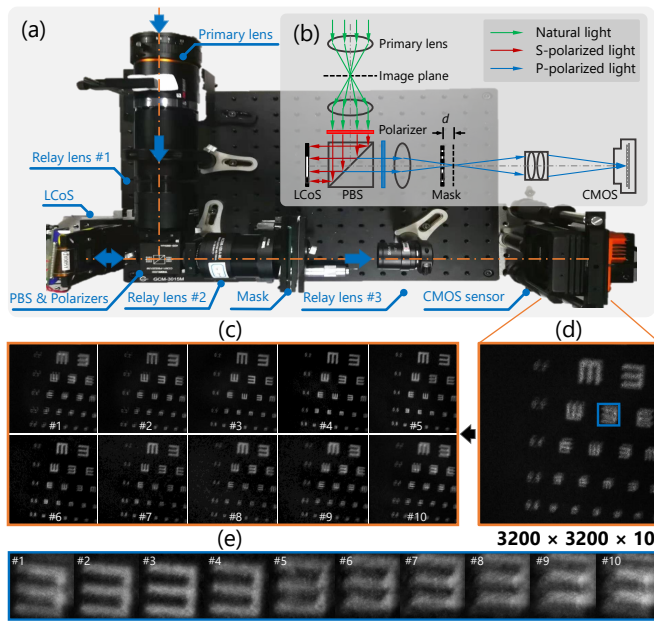


Fig. 1. Our 10-mega pixel video SCI system (a) and the schematic (b). 10 high-speed (200 fps) high-resolution (3200×3200 pixels) video frames (c) reconstructed from a snapshot measurement (d), with motion detail in (e) for the small region in the blue box of (d). Different from existing solutions that only uses an LCoS or a mask (thus with limited spatial resolution), our 10-mega spatio-temporal coding is jointly generated by an LCoS at the aperture plane and a static mask close to the image plane.

snapshot. The high-dimensional data reconstruction in an SCI system can be formulated as an ill-posed linear model. Though different video SCI systems have been built [10, 13–16], they are usually of low spatial resolution. By contrast, in this paper, we aim to build a *high resolution* video SCI system up to 10 mega pixels.

As mentioned above, the 10-mega pixel lenses (including imaging lens and relay lens) and sensors are both commercialized products. Off-the-shelf reconstruction algorithms such as the recently developed plug-and-play (PnP) framework [17, 18] can also meet our demands in most real applications. However, the *10-mega pixel temporally varying mask* is still an open challenge. Classical SCI systems usually rely on shifting masks produced by the lithography technique or dynamic patterns projected by the spatial light modulator (SLM) (such as the digital micromirror device (DMD) or liquid crystal on silicon (LCoS)) as temporally varying masks. The shifting mask scheme can provide high spatial resolution modulation, but it relies on the mechanical movement of the translation stage, which is inaccurate or unstable and can hardly be compact. For the masks generated by SLM or DMD, they can switch quickly with micro-mechanical controllers, but their resolution is generally limited to mega-pixel level, which is difficult to scale up. To the best of our knowledge, there are few SCI systems that can realize 1000×1000 pixel-resolution imaging in real-world scenes [19]. And typically, the resolution in prior works is mostly 256×256 [10] or 512×512 [15]. Therefore, it is desirable to build a high-resolution video SCI system for real applications.

To bridge this research gap, in this paper, we come up with a novel coded aperture imaging scheme, which leverages existing components to achieve the modulation up to 10-mega pixels. Our proposed modulation method is a hybrid approach using both a lithography mask and SLM. As depicted in Fig. 2, during the encoding capture process, two modulation modules, an LCoS and a lithography mask are incorporated

in different planes of the optical system. The LCoS with low spatial resolution is placed at the aperture plane of the imaging system, to dynamically encode the aperture and change the directions of incident lights. And the static lithography mask with high spatial resolution is placed in front of the image plane of the primary lens, which can project different high-resolution patterns on the image plane. When the LCoS changes its patterns, the lights propagating towards the lithography mask will change their directions accordingly, and thus leading to a different pattern. In this manner, we can implement dynamic modulation within one exposure time up to 10-mega pixels. Specifically, this paper makes the following contributions:

- By jointly incorporating a dynamic LCoS and a high resolution lithography mask, we proposed a novel hybrid coded aperture snapshot compressive imaging (HCA-SCI) scheme, which can provide *multiplexed shifting patterns* to encode the image plane without physical movement of the mask.
- Inspired by the plug-and-play (PnP) algorithms for large-scale SCI in [17], we implement a reconstruction algorithm which involves *cascading and series denoising* processes of total variation (TV) [20] denoiser and learning-based FastDVDNet [21] denoiser. Simulation results show that the proposed algorithm can provide relative good reconstruction results in a reasonable time.
- Based on our proposed HCA-SCI scheme and the developed reconstruction algorithm, we build a 10-mega pixel large scale SCI system. Different compression rates of 6, 10, 20, 30 are implemented, providing reconstructed frame rate up to 450 frames per second (fps) for a conventional camera operating at 15 fps, verifying the effectiveness of proposed scheme in real scenarios.

2. RELATED WORK

SCI has been proposed to capture high-dimensional data such as videos and hyper-spectral images from a single low-dimensional coded measurement. The underlying principle is to modulate the scene at a higher frequency than the frame rate of the camera and then the modulated frames are compressively sampled by a low-speed camera. Following this, inverse algorithms are employed to reconstruct the desired high dimensional data [12].

Various video SCI systems have been developed in recent years [10, 13–15, 22–24], and the differences among these implementations mainly lie in the coding strategies. Typically, video SCI systems contain the same components as traditional imaging systems, except for several extra relay lenses and a modulation device that generates temporal-variant masks to encode the image plane. An intuitive approach is to directly use a DMD [15, 22] or an LCoS [13, 14], which can project given patterns with an assigned time sequence, on the image plane for image encoding. A substitute approach in early work is to simply replace the modulation device with a physically shifting lithography mask driven by a piezo [10]. There are also some indirect modulation methods proposed in recent work like [23, 24], which takes advantage of the temporal shifting feature of rolling shutter cameras or streak cameras for the temporal-variant mask generation.

Paralleled to these systems, different algorithms are proposed to improve the SCI reconstruction performance as well. Since the inverse problem is ill-posed, different prior constrains such as TV [25], sparsity [10, 13, 14, 16], self-similarity [26] and Gaussian mixture model (GMM) [27, 28] are employed, forming widely used TwIST [29], GAP-TV [25], DeSCI [26] and some other reconstruction algorithms. Generally, iterative optimization based algorithms have high computational complexity. Inspired by advances of deep learning, some learning-based reconstruction approaches are proposed and boost the reconstruction performance to a large extent [15, 30–34]. Recently,

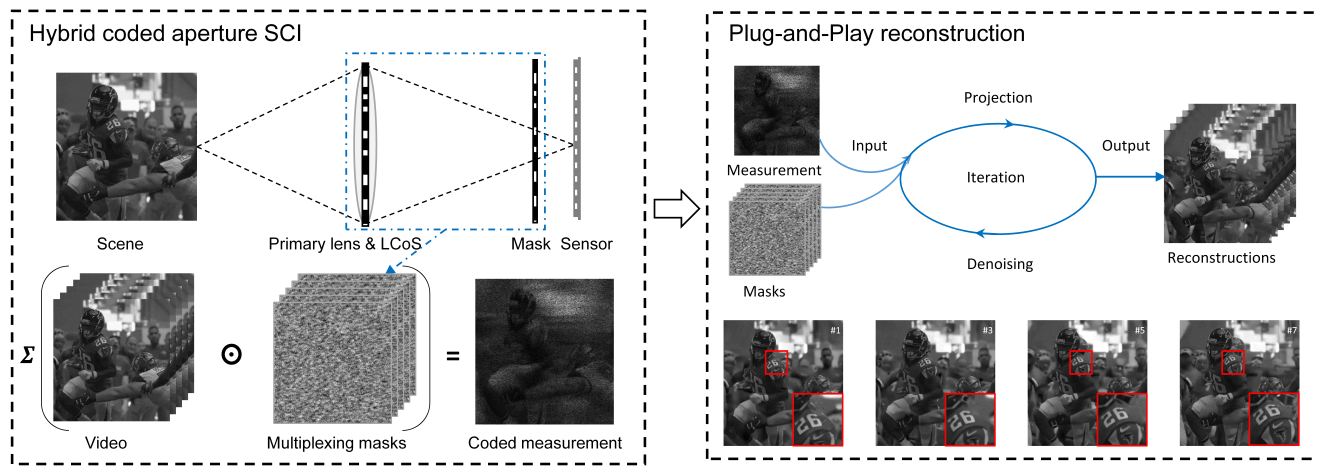


Fig. 2. The pipeline of the proposed large scale hybrid coded aperture snapshot compressive imaging (HCA-SCI) system (left) and the Plug-and-Play (PnP) reconstruction algorithms (right). **Left:** During the encoded photography stage, a dynamic low resolution mask at the aperture plane and a static high resolution mask close to the sensor plane work together to generate a sequence of high resolution codes to encode the large scale video into a snapshot. **Right:** In the decoding, the video is reconstructed under a PnP framework incorporating deep denoising prior into a convex optimization (generalized alternating projection, GAP), which leverages the good convergence of GAP and the high efficiency of the deep network.

a sophisticated reconstruction algorithm BIRNAT [30] based on recurrent neural network (RNN) has led to state-of-the-art reconstruction performance with a significant reduction on the required time compared with DeSCI. However, despite the highest reconstruction quality achieved by learning-based methods, their main limitation lies in the inflexibility resulting from inevitable training process and requirement for large-scale training data when changing encoding masks or data capture environment. Other learning-based methods like MetaSCI [31] try to utilize meta-learning or transfer learning to realize fast mask adaption for SCI reconstruction with different masks, but the time cost is still unacceptable on the 10-mega pixel SCI data. To solve the trilemma of reconstruction quality, time consumption, and algorithm flexibility, a joint framework of iterative and learning-based methods called plug-and-play (PnP) [17] is proposed. By integrating pre-trained deep denoisers as the prior terms into certain iterative optimization process such as generalized alternating projection (GAP) [35] and alternating direction method of multiplier (ADMM) [36], PnP based approaches combine the advantages of both frameworks and realize the trade-off between speed, quality and flexibility.

In this paper, we build a novel video SCI system by using a hybrid coded aperture composed of an LCoS and a physical mask shown in Fig. 1. Moreover, we modify the PnP algorithm to fit our system leading to better results than the method proposed in [17].

3. SYSTEM

A. Hardware implementation

The hardware setup of our HCA-SCI system is depicted in Fig. 1. It consists of a primary lens (HIKROBOT, MVL-LF5040M-F, $f=50\text{mm}$, $F\#=4.0-32$), an amplitude-modulated LCoS (ForthDD, QXGA-3DM, 2048×1536 pixels, 4.5k refresh rate), a lithography mask (5120×5120 pixels, $4.5\mu\text{m} \times 4.5\mu\text{m}$ pixel size), a CMOS camera (HIKROBOT, MV-CH250-20TC, 5120×5120 pixels, $4.5\mu\text{m}$ pixel size), two achromatic doublets (Thorlabs, AC508-075-A-ML, $f=75\text{mm}$), a relay lens (ZLKC, HM5018MP3, $f=50\text{mm}$), a polarizing beamsplitter (Thorlabs, CCM1-PBS251/M), and two film polarizers (Thorlabs, LPVISE100-A). The incident light from a scene is first collected by the primary lens and focused at the first virtual image plane. Then a 4f system consisting of two achromatic doublets transfers the image through the aperture

coding module and the lithography mask, and subsequently onto the second virtual image plane. The aperture coding module positioned at the middle of the 4f system is composed of a polarizing beamsplitter, two film polarizers and an amplitude-modulated LCoS, which are used to change the open-close states ('open' means letting the light go through while 'close' means blocking the light) of the sub-apertures and thus modulate the light's propagation direction. Finally, the image delivered by the 4f system is relayed to the camera sensor being captured. Note that the 4f system used in our system has a magnification of 1, and the relay lens has a magnification of 2, which on the whole provides a 1:2 mapping between pixels of the lithography mask and the sensor. Even though the imaging model involves pixel-wise encoding, there is no need for a precise alignment for the lithography mask and the camera sensor, since the actual encoding mask will be calibrated before data acquisition. During the acquisition process, the camera shutter is synchronized with the LCoS by using an output trigger signal from the LCoS driver board.

It is worth nothing that, the active area of the LCoS and the position of the lithography mask should be carefully adjusted. The active area of the LCoS should be as large as possible meanwhile to ensure it to serve as the aperture stop of the whole system, so that it can provide a higher light efficiency. As for the lithography mask, fine-tune is needed to ensure that the mask's projection on the image plane can generate a shifting when different parts of the aperture is open, and meanwhile, the shifting masks can still keep sharp. In our implementation, after extensive experiments, the mask is placed in front of the second image plane with a distance of $80\mu\text{m}$, which is a good trade-off between the sharpness and the shift.

B. Encoding mask generation

The aperture of the system (*i.e.* the activate area of the LCoS) can be divided into several sub-apertures according to the resolution of the LCoS after pixel binning, and each sub-aperture corresponds to a light beam propagating towards certain directions. As shown in Fig. 3, because the lithography mask is placed in front of the image plane, when different sub-apertures are turned on, the light beams from the corresponding sub-apertures will project the mask onto different parts of the image plane, which can thus generate corresponding shifting encoding masks. In practice, to enhance the light throughput, multi-

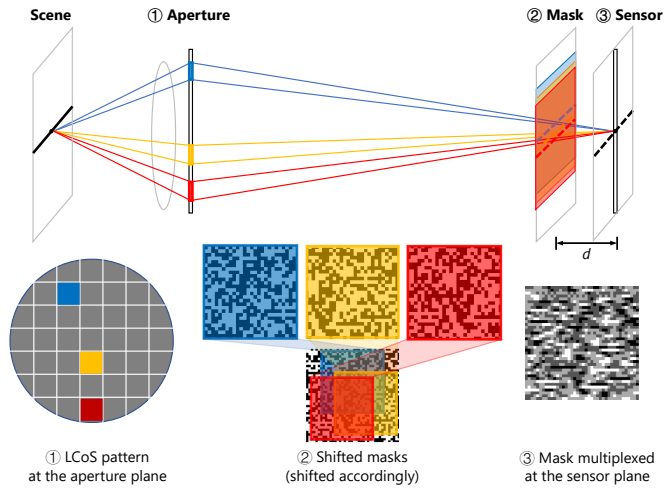


Fig. 3. The illustration of the multiplexed mask generation. For the same scene point, its images generated by different sub-apertures (marked as blue, yellow and red) intersect the mask plane with different regions and thus encoded with corresponding (shifted) random masks before summation at the sensor. The multiplexing would raise the light flux for high signal-to-noise-ratio recording, while with only slight performance degeneration.

ple sub-apertures will be turned on simultaneously in one frame by assigning the LCoS with a specific multiplexing pattern to obtain a single multiplexing encoding mask. And in different frames, different combinations of the sub-apertures are applied to generate different multiplexing encoding masks. Generally, we turn on 50% of the sub-apertures in one multiplexing pattern. In this multiplexing case, the final encoding mask on the image plane will be the summation of those shifting masks provided by the corresponding sub-apertures.

C. Mathematical model

Mathematically, the encoding mask generation process can be modeled as a multiplexing of shifting masks. Let O denote the center-view mask generated by opening the central sub-aperture of the system, then each mask C generated by sub-aperture multiplexing can be formulated as

$$C = \sum_{i=1}^N m_i S_i(O), \quad (1)$$

where S_i denotes the mask shifting operator corresponding to the i -th sub-aperture; m_i is the multiplexing indicator (a scalar) for the i -th sub-aperture, with 0 and 1 for blocking or transmitting the light respectively; and N is the amount of sub-apertures (i.e. the number of macro-pixels in the active area of the LCoS after binning). Consider that a video $X \in \mathbb{R}^{n_x \times n_y \times B}$, containing B consecutive high speed frames is modulated by B encoding masks $C \in \mathbb{R}^{n_x \times n_y \times B}$ and integrated by the sensor to generate a snapshot coded measurement Y . Then Y can be expressed as

$$Y = \sum_{k=1}^B C_k \odot X_k + G, \quad (2)$$

where \odot denotes the Hadamard (element-wise) product; $G \in \mathbb{R}^{n_x \times n_y}$ is the measurement noise; $C_k = C(:, :, k)$ and $X_k = X(:, :, k)$ represent the k -th multiplexed mask and corresponding frame respectively. Through a simple derivation, the coded measurement in Eq. (2) can be further expressed by

$$y = Hx + g, \quad (3)$$

where $y = \text{Vec}(Y) \in \mathbb{R}^n$ and $g = \text{Vec}(G) \in \mathbb{R}^n$ with $n = n_x n_y$. Corresponding video signal $x \in \mathbb{R}^{nB}$ is given by $x = [x_1^T, \dots, x_B^T]^T$, where $x_k = \text{Vec}(X_k) \in \mathbb{R}^n$. Different with traditional CS, the coding matrix

$H \in \mathbb{R}^{n \times nB}$ in video SCI is sparse and has a special structure which can be written as

$$H = [D_1, \dots, D_B], \quad (4)$$

where $D_k = \text{diag}(\text{Vec}(C_b)) \in \mathbb{R}^{n \times n}$. Therefore, the compressive sampling rate in video SCI is equal to $1/B$. Theoretical analysis in [37, 38] has proved that the reconstruction error of SCI is bounded even when $B > 1$.

D. system calibration

Though pixel-wise modulation is involved in SCI systems, there is no need for pixel to pixel alignment during system building, as we can get the precise encoding patterns through an "end-to-end" calibration process before data capture. To be specific, we place a Lambertian white board at the objective plane, and provisionally take away the lithography mask. Then an illumination pattern I and a background pattern B are captured with LCoS projecting white and black patterns, respectively. After that, we put on the lithography mask and capture each dynamic encoding mask C with LCoS projecting corresponding multiplexing patterns directly. To eliminate the influence of background light and nonuniform illumination caused by light source or system vignetting on the actual encoding masks, we conduct calibration to get the accurate encoding mask C' following Eq. (5). Besides, after encoding acquisition, the encoded measurements will also subtract the background pattern to accord with the providing mathematical model, and illumination will be regarded as a part of the scene itself.

$$C' = \frac{C - B}{I - B}, \quad (5)$$

4. RECONSTRUCTION ALGORITHM

The reconstruction of high speed videos from the snapshot coded measurement is an ill-posed problem. As mentioned before, to solve this problem, different priors and frameworks have been employed. Roughly, the algorithms can be categorized into the following 3 classes [12]: *i*) Regularization (or priors) based optimization algorithms with well known methods such as TwIST [29], GAP-TV [25] and De-SCI [26]. *ii*) End-to-end deep learning based algorithms [15, 32, 34], like BIRNAT [30] which reaches state-of-the-art performance and recent developed MetaSCI [31] that using meta-learning to improve adaption capability for different masks in SCI reconstruction. *iii*) Plug-and-Play (PnP) algorithms that using deep denoising networks into the optimization framework such as ADMM and GAP.

Among these algorithms, regularization based algorithms are usually too slow and end-to-end deep learning networks need a large amount of data and also a long time to train the network, in addition to the inflexibility, i.e., re-training being required for a new system. Though recent works like MetaSCI [31] try to mitigate this problem with meta-learning or transfer learning and thus march forward to large-scale SCI problem with patch-wise reconstruction strategy, it still takes a long time for the training and adaption of 10-meta pixel scale SCI reconstruction. For example, MetaSCI takes about two weeks for the $256 \times 256 \times 10$ base model training on a single NVIDIA 2080Ti GPU, and further adaption performed on more than 570 $256 \times 256 \times 10$ sub-tasks (overlapped patches extracted from a 10-mega pixel image) costs about two months, which is impractical in real applications (more GPUs can be used to mitigate this challenge). By contrast, PnP has achieved a well balance of speed, flexibility and accuracy. Therefore, we employ the PnP framework in our work and further develop the PnP-TV-FastDVDNet to achieve promising results for our high-resolution HCA-SCI scheme. Meanwhile, we use GAP-TV and BIRNAT as baselines for comparison purpose.

In the following, we review the main steps of PnP-GAP [17] and then present our PnP-TV-FastDVDNet algorithm for HCA-SCI in Algorithm 1.

A. PnP-GAP

In GAP, the SCI inversion problem is modeled as

$$\arg \min_{x,v} \frac{1}{2} \|x - v\|_2^2 + \lambda R(x), \text{ s.t. } y = Hx, \quad (6)$$

where $R(x)$ is a regularizer or prior being imposed on x , which can be a TV, sparse prior or a deep prior [39] and v is an auxiliary parameter. Let k index the iteration number, through a two-step iteration, the minimization in Eq. (6) can be solved as follows:

- Solving x :

$$x^{(k)} = v^{(k-1)} + H^T (HH^T)^{-1} (y - Hv^{(k-1)}), \quad (7)$$

By utilizing the special structure of H shown in Eq. (4), this sub-problem can be solved efficiently via element-wise operation rather than calculating the inversion of a huge matrix.

- Solving v :

$$v^{(k)} = \mathcal{D}_\sigma(x^{(k)}). \quad (8)$$

where $\mathcal{D}_\sigma(\cdot)$ represents a denoising process with $\sigma = \sqrt{\lambda}$. Here, different denoising algorithms can be used such as TV (thus GAP-TV), WNNM [40] (thus DeSCI [26]) and FFDnet [39] (thus PnP-FFDnet [17]).

B. PnP-TV-FastDVDNet

Recall that solving v following Eq. (8) is equivalent to performing a denoising process on x . By plugging various denoisers into the GAP iteration steps, we can make a trade-off between different aspects of reconstruction performance. In fact, more than one denoiser can be employed in a series manner, i.e. one after another in each iteration; or in a cascading manner, i.e. the first several iterations using one denoiser, while the next several iterations using another. In this way, we can further balance the strengths and drawbacks of different denoisers.

Algorithm 1. PnP-TV-FastDVDNet for HCA-SCI

Require: H, y .

- 1: Initialize: $v^{(0)}, \lambda_0, \xi < 1, k = 1, K_1, K_{Max}$.
- 2: **while** Not Converge **and** $k \leq K_{Max}$ **do**
- 3: Update x by Eq. (7).
- 4: Update v :
- 5: **if** $k \leq K_1$ **then**
- 6: $v^{(k)} = \mathcal{D}_{TV}(x^{(k)})$
- 7: **else**
- 8: $v' = \mathcal{D}_{TV}(x^{(k)})$
- 9: $v^{(k)} = \mathcal{D}_{FastDVDNet}(v')$

In this paper, considering the high video denoising performance of recently proposed FastDVDnet [21], we jointly employ the TV denoiser and the FastDVDNet denoiser in a PnP-GAP framework, implementing a reconstruction algorithm of PnP-GAP-TV+FastDVDNet, which involves cascading and series denoising processes. The algorithm pipeline is shown in Algorithm 1. In each iteration, the updating of x follows Eq. (7), and the updating of v , i.e., the denoising process, differs in different periods. To be specific, in the first period, a single TV denoiser is employed, while in the second period, a joint TV and FastDVDNet denoiser is involved one after another.

5. RESULTS

In this section, we conduct a series of experiments on both simulation data and real data to validate the feasibility and performance of our proposed HCA-SCI system. Four reconstruction algorithms including iterative optimization based algorithm GAP-TV [25], plug-and-play based algorithm PnP-FFDNet [17], our proposed PnP-TV-FastDVDNet, and the state-of-the-art learning-based algorithm BIRNAT [30] are employed.

A. Multiplexing pattern design

Multiplexing pattern design plays an important role in our HCA-SCI system. In simulation, we used the "random squares" multiplexing scheme (shown in the first row of Fig. 4), which contains 12 sub-apertures with each sub-aperture containing 512×512 binning pixels. In each multiplexing pattern, there are 50% randomly selected sub-apertures being "open". In real experiments, the optical aberration and diffraction that are not considered in simulation experiments will cause blur to the encoding mask, and thus introduce more correlation among the encoding masks which degrades the encoding effect. Considering the fact that the calibration process is conducted in an "end-to-end" manner in real experiments, we thus have enough degree of freedom to design any possible multiplexing patterns without being limited by the binning mode or the sub-aperture amount. We empirically tried many different schemes, and finally found that the "rotating circle" scheme (shown in the second row of Fig. 4) can realized a good balance between the system's light throughput and the encoding masks' quality when taking the physical factors into account.

Currently, the design of the multiplexing patterns is heuristic, and the challenge of the algorithm-based multiplexing pattern design mainly lies in the large size of the multiplexing pattern (1536×2048) and the video data (10-mega) in our system. Both traditional optimization-based methods and learning based methods have difficulty in dealing with data of this scale. So, the design of the optimal multiplexing pattern is still an open challenge which is worthy for future investigation.

B. Reconstruction comparison between different algorithms on simulation datasets

In order to investigate the reconstruction performance of different algorithms on the proposed HCA-SCI system, we first perform experiments on simulated datasets, which involve three different scales of 256×256 , 512×512 , 1024×1024 and two compressive rates (Cr) of 10 and 20. Two datasets named Football and Hummingbird used in [17] and three datasets named ReadySteadyGo, Jockey and YachtRide provided in [41] are employed in our simulation. According to the forward model depicted in Section C, to simulate the encoding masks, we first

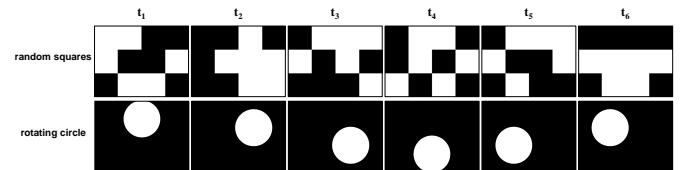


Fig. 4. Multiplexing pattern schemes used in our experiments (taking Cr = 6 for an example). **Top row:** multiplexing patterns for simulation experiments. Each pattern contains 50% "open" sub-apertures, and each sub-apertures is a 512×512 binning macro pixel on the LCoS. **Bottom row:** multiplexing patterns for real experiments. Each pattern contains an "open" circle with a radius of about 400 pixels, and the circles in adjacent patterns have a rotation of $360/\text{Cr}$ degrees.

Table 1. The average results of PSNR in dB (left entry in each cell) and SSIM (right entry in each cell) by different algorithms (Cr = 10). BIRNAT fails at large-scale due to limited GPU memory.

Scales	Algorithms	Football	Hummingbird	ReadySteadyGo	Jockey	YachtRide	Average
256 × 256	GAP-TV	27.82, 0.8280	29.24, 0.7918	23.73, 0.7499	31.63, 0.8712	26.65, 0.8056	27.81, 0.8093
	PnP-FFDNet	27.06, 0.8264	25.52, 0.6912	21.68, 0.6859	31.14, 0.8493	23.69, 0.7035	25.82, 0.7513
	PnP-TV-FastDVDNet	31.31, 0.9123	31.19, 0.8264	26.18, 0.8276	31.36, 0.8817	28.90, 0.8841	29.79, 0.8664
	BIRNAT	34.67, 0.9719	34.33, 0.9546	29.50, 0.9389	36.24, 0.9711	31.02, 0.9431	33.15, 0.9559
512 × 512	GAP-TV	29.19, 0.8854	28.32, 0.7887	25.94, 0.7918	31.30, 0.8718	26.59, 0.7939	28.27, 0.8263
	PnP-FFDNet	28.57, 0.8952	28.02, 0.8363	24.32, 0.7457	29.81, 0.8248	23.45, 0.6793	26.83, 0.7963
	PnP-TV-FastDVDNet	30.92, 0.9333	32.24, 0.8834	27.04, 0.8246	32.11, 0.8839	27.87, 0.8487	30.04, 0.8748
	BIRNAT	34.67, 0.9719	34.33, 0.9546	29.50, 0.9389	36.24, 0.9711	31.02, 0.9431	33.15, 0.9559
1024 × 1024	GAP-TV	30.63, 0.9022	29.16, 0.8459	28.92, 0.8698	31.59, 0.8953	29.03, 0.8470	29.87, 0.8720
	PnP-FFDNet	29.87, 0.9023	27.70, 0.7869	27.70, 0.8483	29.88, 0.8412	25.55, 0.7211	28.14, 0.8200
	PnP-TV-FastDVDNet	30.35, 0.9265	31.71, 0.8909	29.42, 0.8913	31.59, 0.9014	30.44, 0.8713	30.70, 0.8963
	BIRNAT	34.67, 0.9719	34.33, 0.9546	29.50, 0.9389	36.24, 0.9711	31.02, 0.9431	33.15, 0.9559

Table 2. The average results of PSNR in dB (left entry in each cell) and SSIM (right entry in each cell) by different algorithms (Cr = 20). BIRNAT fails at large-scale due to limited GPU memory.

Scales	Algorithms	Football	Hummingbird	ReadySteadyGo	Jockey	YachtRide	Average
256 × 256	GAP-TV	25.01, 0.7544	26.33, 0.6893	20.48, 0.6326	28.13, 0.8318	23.56, 0.7129	24.70, 0.7242
	PnP-FFDNet	21.67, 0.6657	22.13, 0.5835	17.27, 0.5340	27.78, 0.7994	20.39, 0.6024	21.85, 0.6370
	PnP-TV-FastDVDNet	27.83, 0.8459	28.65, 0.7520	23.28, 0.7381	29.51, 0.8597	26.34, 0.8235	27.12, 0.8038
	BIRNAT	27.91, 0.9021	28.58, 0.8800	23.79, 0.8279	31.35, 0.9467	26.14, 0.8585	27.55, 0.8830
512 × 512	GAP-TV	23.97, 0.8179	24.50, 0.6719	22.12, 0.6975	26.99, 0.8297	23.13, 0.6930	24.14, 0.7420
	PnP-FFDNet	22.00, 0.7661	23.62, 0.7245	19.35, 0.6133	25.32, 0.7924	19.48, 0.5418	21.95, 0.6876
	PnP-TV-FastDVDNet	25.63, 0.8852	28.36, 0.7778	23.80, 0.7499	28.79, 0.8553	25.36, 0.7784	26.39, 0.8093
	BIRNAT	27.91, 0.9021	28.58, 0.8800	23.79, 0.8279	31.35, 0.9467	26.14, 0.8585	27.55, 0.8830
1024 × 1024	GAP-TV	24.82, 0.8353	25.53, 0.7296	24.98, 0.8128	26.63, 0.8388	25.80, 0.7759	25.55, 0.7985
	PnP-FFDNet	23.55, 0.8098	23.02, 0.6039	22.48, 0.7702	24.48, 0.7968	21.67, 0.6414	23.04, 0.7244
	PnP-TV-FastDVDNet	26.26, 0.8729	28.68, 0.8076	26.31, 0.8399	29.18, 0.8773	28.07, 0.8194	27.70, 0.8434
	BIRNAT	27.91, 0.9021	28.58, 0.8800	23.79, 0.8279	31.35, 0.9467	26.14, 0.8585	27.55, 0.8830

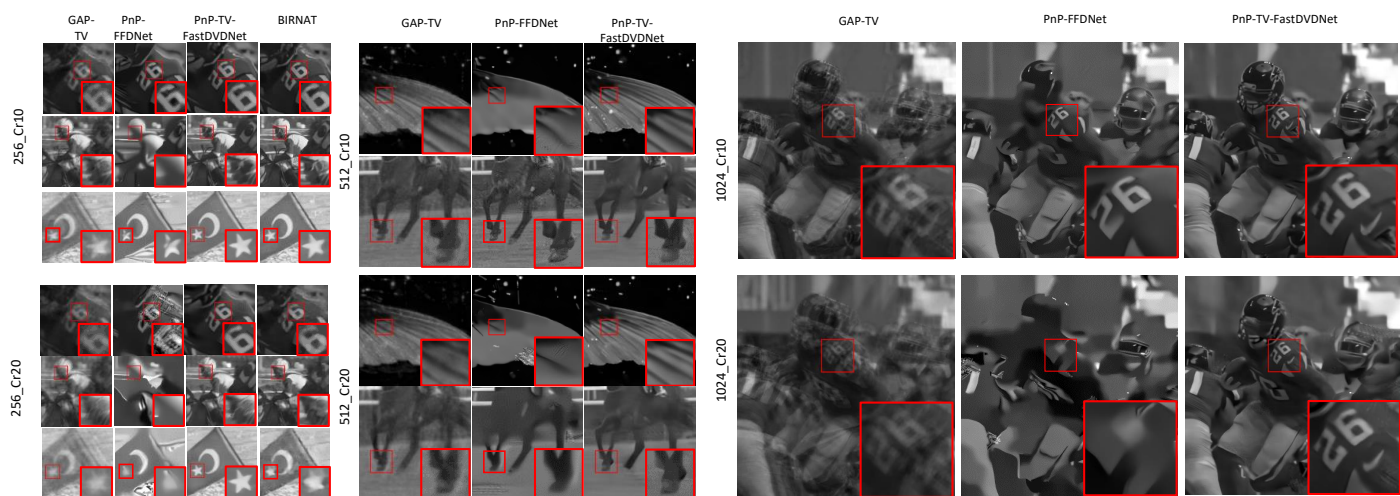


Fig. 5. Reconstruction results and comparison with state-of-the-art algorithms on simulated data at different resolutions (left: 256×256, middle: 512×512, right: 1024×1024) and with different compression ratios (top: Cr = 10, bottom: Cr = 20). The BIRNAT results are not available for 512×512 and 1024×1024 since the model training will be out of memory. See Visualization 1-6 for the reconstructed videos.

371 calculate the mask shifting distance with respect to the center-view
372 mask for each sub-aperture in the current multiplexing pattern (shown
373 in the first row of Fig. 4) based on geometry optics. Then we shift
374 the center-view mask accordingly to get each sub-aperture's shifting
375 mask. And finally the shifting masks are added together to obtain the
376 final multiplexing encoding mask on the image plane. After that, we
377 can generate six groups of simulation datasets by modulating different
378 scales of videos (containing 10 or 20 frames) with multiplexed shifting
379 masks generated from the HCA-SCI system and then collapsing the
380 coded frames to a single (coded) measurement.

381 The reconstruction PSNR and SSIM for each algorithm are summa-
382 rized in Table 1 and Table 2 for Cr = 10 and 20, respectively. It is worth
383 nothing that due to the limited memory of our GPU (GeForce RTX
384 3090 with 24GB memory), we only test BIRNAT on 256×256 scale
385 datasets with Cr equaling to 10 and 20, and the adversarial training is
386 not involved. For GAP-TV and PnP-TV-FastDVDNet, the reconstruction
387 is conducted on a platform equipped with a Intel(R) Core(TM) i7-
388 9700K CPU (3.60GHz, 32G memory) and a GeForce RTX 2080 GPU
389 with 8G memory; 160 and 250 iterations are taken for Cr = 10 and 20,
390 respectively. It can be observed that: *i*) On all six groups of simulated
391 datasets, our proposed PnP-TV-FastDVDNet outperforms GAP-TV
392 and PnP-FFDNet for about 1.5dB and 4dB on average, respectively.
393 *ii*) On the 256_Cr10 and 256_Cr20 datasets, BIRNAT leads the best
394 performance (with sufficient training) exceeding PnP-TV-FastDVDNet
395 for about 3.4dB and 0.4dB, respectively. *iii*) BIRNAT is the fastest al-
396 gorithm during inference period with hundreds times shorter time than
397 GAP-TV and PnP-TV-FastDVDNet. However, the training process
398 of BIRNAT is quite time-consuming, and it takes about one week to
399 train the network without adversarial training for 25 epochs. *iv*) From
400 the selected reconstruction video frames in Fig. 5, we can see that our
401 proposed PnP-TV-FastDVDnet provides higher visualization quality
402 with sharp edges and less artifacts. By contrast, GAP-TV produces
403 noisy results while PnP-FFDnet leads to some unpleasant artifacts.

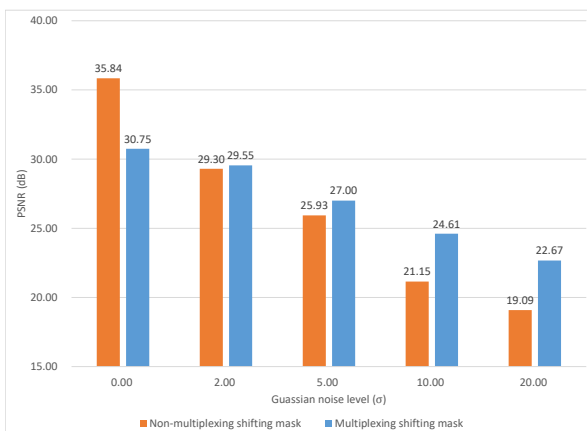


Fig. 6. Noise robustness comparison between multiplexed masks and non-multiplexed masks.

C. Validation of multiplexed shifting mask's noise robustness on simulation datasets

404 As mentioned in Section B, our proposed HCA-SCI system leverages
405 multiplexing strategy for the improvement of light throughput, which
406 can thus gain a higher signal to noise ration (SNR) and enhance the sys-
407 tem's robustness to noise in real-world applications. In this subsection,
408 we conduct a series of experiments on simulation datasets containing
409 different level of noise to compare the reconstruction performance of
410 multiplexed shifting masks used in HCA-SCI and non-multiplexed
411

412 ones. The 256×256 size dataset mentioned above are utilized here as
413 the clean original frames. And we normalize the masks with a light
414 throughput factor calculating from the proportion of the masks' active
415 area with respect to the whole aperture. Zero-mean Gaussian noise
416 with standard deviation ranging from 0 to 20 is added to the measure-
417 ments (with values in $[0, 255]$) to simulate the real-world acquisition
418 process.

419 The change of reconstruction PSNR over increasing noise levels
420 is shown in Fig. 6. As can be seen from the figure, shifting masks
421 with no multiplexing outperform the multiplexed ones when there is no
422 noise, which is probably because the multiplexing operation brings in
423 some correlation among the masks that is not desired for the encoding
424 and reconstruction. However, as the noise increases, the superiority
425 in SNR of the multiplexing scheme shows up, and the reconstruction
426 PSNR of non-multiplexed shifting masks drops rapidly, while that of
427 the multiplexed masks decreases more slowly and exceeds the PSNR
428 of the non-multiplexed ones. In real scenes, noise is inevitable, and
429 as the noise get larger, it will also impose significant impact on the
430 reconstruction process until totally disrupt the reconstruction. So the
431 multiplexing strategy leveraged in HCA-SCI can equip the physical
432 system with more robustness in real applications, especially those at
433 relatively large noise levels.

D. Real data results

434 We build a 10-mega-pixel snapshot compressive camera prototype
435 illustrated in Fig. 1 for dynamic video recording. Empirically, the
436 multiplexing patterns (shown in the second row of Fig. 4) projected
437 by the LCoS are designed to be rotationally symmetric which ensures
438 the consistency in the final coding patterns and provides adequate
439 incoherence among these masks. Before acquisition, we first calibrate
440 the groups of coding masks with a Lambertian whiteboard placed at
441 the objective plane, and each calibrated pattern is averaged over 50
442 repetitive snapshots to suppress the sensor noise. Then, during data
443 capture, the camera operates at a fixed frame rate of 20 fps when Cr =
444 6, 10, and 20, providing reconstruction video frame rate of 120, 200
445 and 400 fps, respectively. For Cr = 30, the camera operates at 15 fps to
446 extend the exposure time and provide a higher light throughput, which
447 can reach a reconstruction frame rate up to 450 fps. We determine the
448 spatial resolution of our system as 3200×3200 pixels. We thus have
449 achieved the throughput of 4.6G voxels per second in the reconstructed
450 video.

451 Three moving test charts printed on A4 papers are chosen as the
452 dynamic objects. In Fig. 7, we show the coded measurements and final
453 reconstruction of the test charts. From which, one can see that the
454 proposed HCA-SCI system and PnP-GAP-FastDVDNet reconstruction
455 algorithm can effectively capture and restore the moving details of
456 dynamic objects, which will be blurry when captured directly with
457 conventional cameras. For the reconstruction of real data, we also find
458 that, in some cases, the start and end frames tend to be blurry (refer
459 to real data results of Cr = 10 and Cr = 30 in Fig. 7), which might
460 be caused by the synchronization imperfection and initialization delay of
461 the LCoS when switching between the projection sequences.

462 We further compare the reconstruction of GAP-TV, PnP-FFDNet
463 and PnP-TV-FastDVDNet on real datasets captured by our HCA-SCI
464 system. From the reconstruction results shown in Fig. 8, we can
465 find that when Cr = 6, all these three algorithms can produce clear
466 reconstruction frames with sharp details especially in the intermediate
467 frames. But when Cr gets larger, the reconstructed frames of GAP-
468 TV tend to be blurry and have more background noise. PnP-FFDNet
469 will generate severe artifacts in the reconstructed frames and make
470 the motion invisible. But our proposed PnP-TV-FastDVDNet can still
471 reconstruct the motion details with a little increasing of noise in the
472 background.

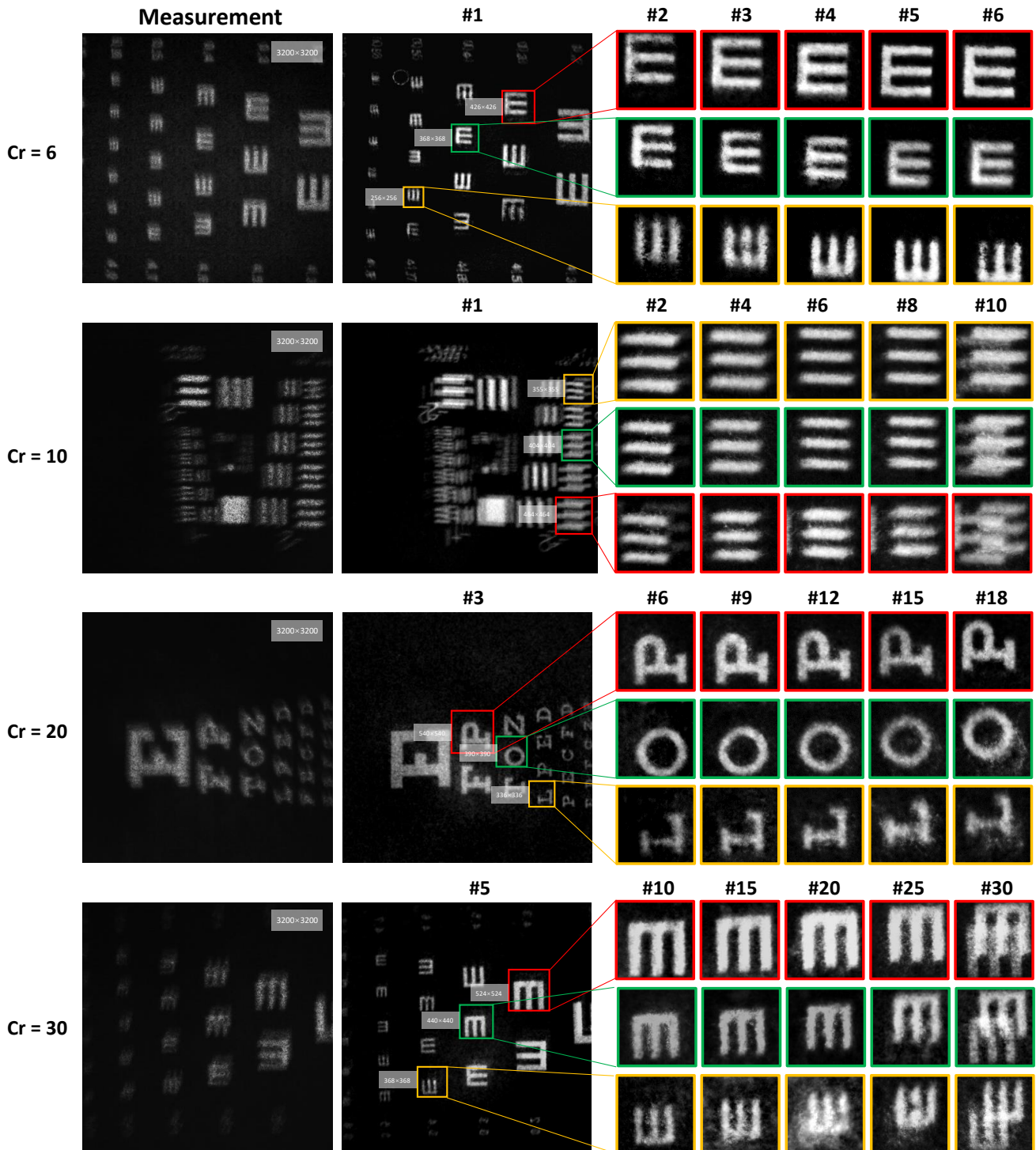


Fig. 7. Reconstruction results of PnP-TV-FastDVDNet on real data captured by our HCA-SCI system ($Cr = 6, 10, 20$ and 30). Note the full frames are of 3200×3200 and we plot small regions of sizes around 400×400 to demonstrate the high-speed motion.

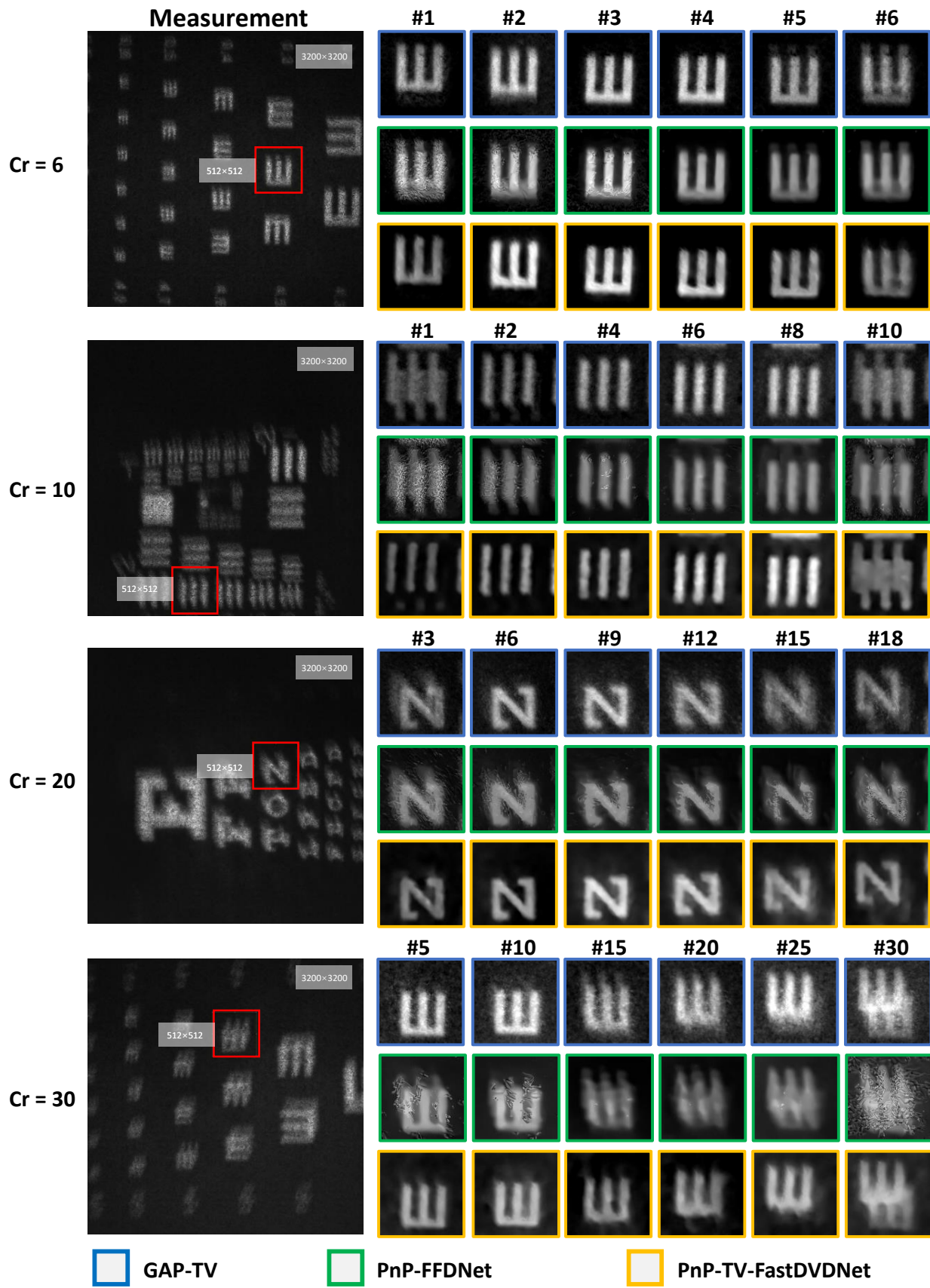


Fig. 8. Reconstruction comparison between GAP-TV, PnP-FFDNet and PnP-TV-FastDVDNet on real data captured by our HCA-SCI system (Cr = 6, 10, 20 and 30). Note the full frames are of 3200x3200 and we plot small regions of size of 512x512 to demonstrate the high-speed motion. See Visualization 7 for the reconstructed videos.

6. CONCLUSION

We have proposed a new computational imaging scheme capable of capturing 10 mega-pixel videos with low bandwidth and developed corresponding algorithms for computational reconstruction, providing a high throughput (up to 4.6G voxels per second) solution for high-speed, high-resolution videos.

The hardware design bypasses the pixel count limitation of available spatial light modulators via joint coding at aperture and close to image plane. The results demonstrate the feasibility of high throughput imaging under snapshot compressive sensing scheme and hold great potential for future applications in industrial visual inspection or multi-scale surveillance.

So far, the final reconstruction is limited to 450Hz since the hybrid coding scheme further decreases the light throughput to some extent compared with conventional coding strategies. In the future, a worthwhile extension is to introduce new photon-efficient aperture coding devices to raise the signal-to-noise ratio for coded measurements. Another limitation of the current system lies in the non uniformity of the encoding masks along the radial direction, which is a common problem for large-scale imaging systems due to non-negligible off-axis aberration. Considering the challenge for improving optical performance of existing physical components, designing novel algorithms which are capable of SCI reconstruction with non-uniform masks may be an economical and feasible way. Meanwhile, time-efficient reconstruction algorithms and feasible multiplexing pattern design methods for large-scale (like 10-mega pixel or even Giga pixel) SCI reconstruction is still an open challenge in the foreseeable future. Besides, extending proposed imaging scheme for higher throughput (e.g., Giga-pixel) or other dimensions (e.g., light field, hyperspectral imaging) may also be a promising direction.

Funding. Ministry of Science and Technology of the People's Republic of China (Grant No. 2020AAA0108202); National Natural Science Foundation of China (Grant Nos. 61931012, 62088102).

Acknowledgments. Zhihong Zhang and Chao Deng (marked with † in the author list) contributed equally to this paper.

Disclosures. X. Y., Nokia (E).

Data Availability Statement. Data underlying the results presented in this paper are not publicly available at this time but may be obtained from the authors upon reasonable request.

REFERENCES

- G. Carles, J. Downing, and A. R. Harvey, "Super-resolution imaging using a camera array," *Opt. letters* **39**, 1889–1892 (2014).
- S. Farsiu, M. D. Robinson, M. Elad, and P. Milanfar, "Fast and robust multiframe super resolution," *IEEE Transactions on Image Process.* **13**, 1327–1344 (2004).
- R. F. Marcia and R. M. Willett, "Compressive coded aperture superresolution image reconstruction," in *2008 IEEE International Conference on Acoustics, Speech and Signal Processing (ICASSP)*, (IEEE, Las Vegas, NV, USA, 2008), pp. 833–836.
- T. S. Cho, A. Levin, F. Durand, and W. T. Freeman, "Motion blur removal with orthogonal parabolic exposures," in *2010 IEEE International Conference on Computational Photography (ICCP)*, (IEEE, Cambridge, MA, USA, 2010), pp. 1–8.
- R. Raskar, A. Agrawal, and J. Tumblin, "Coded exposure photography: Motion deblurring using fluttered shutter," *ACM Transactions on Graph.* **25**, 795–804 (2006).
- C. Zhou and S. Nayar, "What are good apertures for defocus deblurring?" in *2009 IEEE International Conference on Computational Photography (ICCP)*, (IEEE, San Francisco, CA, USA, 2009), pp. 1–8.
- C. Zhou, S. Lin, and S. K. Nayar, "Coded Aperture Pairs for Depth from Defocus and Defocus Deblurring," *Int. J. Comput. Vis.* **93**, 53–72 (2011).
- A. Sellent and P. Favaro, "Optimized aperture shapes for depth estimation," *Pattern Recognit. Lett.* **40**, 96–103 (2014).
- S. Suwajanakorn, C. Hernandez, and S. M. Seitz, "Depth from focus with your mobile phone," in *2015 IEEE Conference on Computer Vision and Pattern Recognition (CVPR)*, (IEEE, Boston, MA, USA, 2015), pp. 3497–3506.
- P. Llull, X. Liao, X. Yuan, J. Yang, D. Kittle, L. Carin, G. Sapiro, and D. J. Brady, "Coded aperture compressive temporal imaging," *Opt. Express* **21**, 10526 (2013).
- A. Wagadarikar, R. John, R. Willett, and D. Brady, "Single disperser design for coded aperture snapshot spectral imaging," *Appl. Opt.* **47**, B44 (2008).
- X. Yuan, D. J. Brady, and A. K. Katsaggelos, "Snapshot compressive imaging: Theory, algorithms, and applications," *IEEE Signal Process. Mag.* **38**, 65–88 (2021).
- D. Reddy, A. Veeraraghavan, and R. Chellappa, "P2C2: Programmable pixel compressive camera for high speed imaging," in *2011 IEEE Conference on Computer Vision and Pattern Recognition (CVPR)*, (IEEE, Colorado Springs, CO, USA, 2011), pp. 329–336.
- Y. Hitomi, J. Gu, M. Gupta, T. Mitsunaga, and S. K. Nayar, "Video from a single coded exposure photograph using a learned over-complete dictionary," in *2011 International Conference on Computer Vision (ICCV)*, (IEEE, Barcelona, Spain, 2011), pp. 287–294.
- M. Qiao, Z. Meng, J. Ma, and X. Yuan, "Deep learning for video compressive sensing," *APL Photonics* **5**, 030801 (2020).
- X. Yuan, P. Llull, X. Liao, J. Yang, D. J. Brady, G. Sapiro, and L. Carin, "Low-Cost Compressive Sensing for Color Video and Depth," in *2014 IEEE Conference on Computer Vision and Pattern Recognition (CVPR)*, (IEEE, Columbus, OH, USA, 2014), pp. 3318–3325.
- X. Yuan, Y. Liu, J. Suo, and Q. Dai, "Plug-and-Play Algorithms for Large-Scale Snapshot Compressive Imaging," in *2020 IEEE/CVF Conference on Computer Vision and Pattern Recognition (CVPR)*, (IEEE, Seattle, WA, USA, 2020), pp. 1444–1454.
- X. Yuan, Y. Liu, J. Suo, F. Durand, and Q. Dai, "Plug-and-play algorithms for video snapshot compressive imaging," *IEEE Transactions on Pattern Analysis Mach. Intell.* pp. 1–1 (2021).
- Y. Sun, X. Yuan, and S. Pang, "Compressive high-speed stereo imaging," *Opt. Express* **25**, 18182 (2017).
- L. I. Rudin, S. Osher, and E. Fatemi, "Nonlinear total variation based noise removal algorithms," *Phys. D: Nonlinear Phenom.* **60**, 259–268 (1992).
- M. Tassano, J. Delon, and T. Veit, "FastDVDnet: Towards Real-Time Deep Video Denoising Without Flow Estimation," in *2020 IEEE/CVF Conference on Computer Vision and Pattern Recognition (CVPR)*, (IEEE, Seattle, WA, USA, 2020), pp. 1351–1360.
- C. Deng, Y. Zhang, Y. Mao, J. Fan, J. Suo, Z. Zhang, and Q. Dai, "Sinusoidal sampling enhanced compressive camera for high speed imaging," *IEEE Transactions on Pattern Analysis Mach. Intell.* **43**, 1380–1393 (2021).
- L. Gao, J. Liang, C. Li, and L. V. Wang, "Single-shot compressed ultrafast photography at one hundred billion frames per second," *Nature* **516**, 74–77 (2014).
- N. Antipa, P. Oare, E. Bostan, R. Ng, and L. Waller, "Video from Stills: Lensless Imaging with Rolling Shutter," in *2019 IEEE International Conference on Computational Photography (ICCP)*, (IEEE, Tokyo, Japan, 2019), pp. 1–8.
- X. Yuan, "Generalized alternating projection based total variation minimization for compressive sensing," in *2016 IEEE International Conference on Image Processing (ICIP)*, (IEEE, Phoenix, AZ, USA, 2016), pp. 2539–2543.
- Y. Liu, X. Yuan, J. Suo, D. Brady, and Q. Dai, "Rank minimization for snapshot compressive imaging," *IEEE Transactions on Pattern Analysis Mach. Intell.* **41**, 2990–3006 (2019).
- J. Yang, X. Yuan, X. Liao, P. Llull, D. J. Brady, G. Sapiro, and L. Carin, "Video Compressive Sensing Using Gaussian Mixture Models," *IEEE Transactions on Image Process.* **23**, 4863–4878 (2014).
- Jianbo Yang, Xuejun Liao, Xin Yuan, P. Llull, D. J. Brady, G. Sapiro, and L. Carin, "Compressive Sensing by Learning a Gaussian Mixture

- 605 Model From Measurements,” *IEEE Transactions on Image Process.* **24**,
606 106–119 (2015).
- 607 29. J. Bioucas-Dias and M. Figueiredo, “A New TwIST: Two-Step Iterative
608 Shrinkage/Thresholding Algorithms for Image Restoration,” *IEEE*
609 *Transactions on Image Process.* **16**, 2992–3004 (2007).
- 610 30. Z. Cheng, R. Lu, Z. Wang, H. Zhang, B. Chen, Z. Meng, and X. Yuan,
611 “BIRNAT: Bidirectional recurrent neural networks with adversarial training
612 for video snapshot compressive imaging,” in *Computer Vision –*
613 *ECCV 2020*, A. Vedaldi, H. Bischof, T. Brox, and J.-M. Frahm, eds.
614 (Springer International Publishing, Cham, 2020), pp. 258–275.
- 615 31. Z. Wang, H. Zhang, Z. Cheng, B. Chen, and X. Yuan, “Metasci: Scalable
616 and adaptive reconstruction for video compressive sensing,” in
617 *2021 IEEE/CVF Conference on Computer Vision and Pattern Recognition*
618 *(CVPR)*, (2021), pp. 2083–2092.
- 619 32. M. Iliadis, L. Spinoulas, and A. K. Katsaggelos, “Deep fully-connected
620 networks for video compressive sensing,” *Digit. Signal Process.* **72**,
621 9–18 (2018).
- 622 33. K. Kulkarni, S. Lohit, P. Turaga, R. Kerviche, and A. Ashok, “ReconNet:
623 Non-Iterative Reconstruction of Images from Compressively Sensed
624 Measurements,” in *2016 IEEE Conference on Computer Vision and*
625 *Pattern Recognition (CVPR)*, (IEEE, Las Vegas, NV, USA, 2016), pp.
626 449–458.
- 627 34. J. Ma, X.-Y. Liu, Z. Shou, and X. Yuan, “Deep Tensor ADMM-Net
628 for Snapshot Compressive Imaging,” in *2019 IEEE/CVF International*
629 *Conference on Computer Vision (ICCV)*, (IEEE, Seoul, Korea (South),
630 2019), pp. 10222–10231.
- 631 35. X. Liao, H. Li, and L. Carin, “Generalized Alternating Projection for
632 Weighted- $\ell_{2,1}$ Minimization with Applications to Model-Based
633 Compressive Sensing,” *SIAM J. on Imaging Sci.* **7**, 797–823 (2014).
- 634 36. S. Boyd, N. Parikh, E. Chu, B. Peleato, and J. Eckstein, “Distributed
635 optimization and statistical learning via the alternating direction method
636 of multipliers,” *Foundations Trends Mach. Learn.* **3**, 1–122 (2011).
- 637 37. S. Jalali and X. Yuan, “Compressive Imaging Via One-Shot Measure-
638 ments,” in *2018 IEEE International Symposium on Information Theory*,
639 (IEEE, 2018).
- 640 38. S. Jalali and X. Yuan, “Snapshot Compressed Sensing: Performance
641 Bounds and Algorithms,” *IEEE Transactions on Inf. Theory* **65**, 8005–
642 8024 (2019).
- 643 39. K. Zhang, W. Zuo, and L. Zhang, “FFDNet: Toward a fast and flexible
644 solution for CNN based image denoising,” *IEEE Transactions on Image*
645 *Process.* **27**, 4608–4622 (2018).
- 646 40. S. Gu, L. Zhang, W. Zuo, and X. Feng, “Weighted Nuclear Norm
647 Minimization with Application to Image Denoising,” in *2014 IEEE Con-*
648 *ference on Computer Vision and Pattern Recognition (CVPR)*, (IEEE,
649 Columbus, OH, USA, 2014), pp. 2862–2869.
- 650 41. A. Mercat, M. Viitanen, and J. Vanne, “UVG dataset: 50/120fps 4K
651 sequences for video codec analysis and development,” in *Proceedings*
652 *of the 11th ACM Multimedia Systems Conference*, (ACM, Istanbul
653 Turkey, 2020), pp. 297–302.